

# Spin-resolved electronic structure of ferromagnetic triple-layered ruthenate $\text{Sr}_4\text{Ru}_3\text{O}_{10}$

Prosper Ngabonziza,<sup>1,2,\*</sup> Jonathan D. Denlinger,<sup>3,†</sup> Alexei V. Fedorov,<sup>3</sup>  
Gang Cao,<sup>4</sup> J. W. Allen,<sup>5</sup> G. Gebreyesus,<sup>6</sup> and Richard M. Martin<sup>7,8</sup>

<sup>1</sup>*Department of Physics and Astronomy, Louisiana State University, Baton Rouge, LA 70803, USA*

<sup>2</sup>*Department of Physics, University of Johannesburg,*

*P.O. Box 524 Auckland Park 2006, Johannesburg, South Africa*

<sup>3</sup>*Advanced Light Source, Lawrence Berkeley National Laboratory, Berkeley, California 94720, USA*

<sup>4</sup>*Department of Physics, University of Colorado at Boulder, Boulder, Colorado 80309, USA*

<sup>5</sup>*Randall Laboratory of Physics, University of Michigan, Ann Arbor, Michigan 48109, USA*

<sup>6</sup>*Department of Physics, School of Physical and Mathematical Sciences,  
College of Basic and Applied Sciences, University of Ghana, Ghana*

<sup>7</sup>*Department of Physics, University of Illinois at Urbana-Champaign, Urbana, Illinois 61801, USA*

<sup>8</sup>*Department of Applied Physics, Stanford University, Stanford, California 94305, USA*

(Dated: May 15, 2023)

High-resolution angle- and spin-resolved photoemission spectroscopy reveals new features of the electronic structure of the ferromagnetic triple-layered ruthenate  $\text{Sr}_4\text{Ru}_3\text{O}_{10}$ . There are narrow spectral peaks  $\sim 30$  meV below the Fermi-level in two regions of the Brillouin zone: a hole-like band at the zone-center and a saddle-point van Hove singularity at the zone edge. Below  $T_c$  each feature is almost completely spin-polarized, with opposite sign polarization and with strong Kondo-coherence-like temperature-dependent spectral weight variation suggestive of strong Hund's metal correlations. In addition, there are distinct Fermi surfaces for wide electron-like minority spin bands around the zone center and narrow hole-like majority spin Fermi surface contours around the zone corners. The origin of these features is in general agreement with density functional calculations, if they are shifted to reduce the exchange splitting, and scaled to take into account effects of correlation. Furthermore, the deduced narrow band origins from the tri-layer splitting of  $d_{xz/yz}$  orbitals implies a layer-specific spin-polarization contribution from the narrow bands. Over a larger energy range, net spin-majority polarization of incoherent Ru  $d$ -bands is observed to extend down to the top of the oxygen bands, where additional narrow oxygen bands contribute to the magnetism with spin-minority polarization.

## Introduction

Strontium ruthenates of the Ruddlesden-Popper phases  $\text{Sr}_{n+1}\text{Ru}_n\text{O}_{3n+1}$  ( $n = 1, 2, 3, \dots, \infty$ ) play a pivotal role in studies of strongly correlated electron systems. Depending on the number  $n$  of the  $\text{RuO}_6$  octahedra layers in the unit cell, they exhibit phenomena ranging from unconventional superconductivity in  $\text{Sr}_2\text{RuO}_4$  ( $n=1$ ) [1], quantum critical metamagnetism and nematic fluid with heavy  $d$ -electron masses in  $\text{Sr}_3\text{Ru}_2\text{O}_7$  ( $n=2$ ) [2, 3], and anisotropic ferromagnetism and in-plane metamagnetism in  $\text{Sr}_4\text{Ru}_3\text{O}_{10}$  ( $n=3$ ) [4–7]. The limit of  $n = \infty$  is the three-dimensional ferromagnetic crystal  $\text{SrRuO}_3$ . It has often been considered to be an itinerant ferromagnet [8], but there is evidence of localized correlated behavior [9]. This rich array of distinct collective phenomena can be traced to the competition between local and itinerant behaviors, effects of dimensionality, structural distortions, orbital polarization, crystal field splitting and spin-orbit coupling [10]. In all these materials electronic correlation and magnetism play key roles.

The electronic structure of the single-layer  $\text{Sr}_2\text{RuO}_4$  and double-layer  $\text{Sr}_3\text{Ru}_2\text{O}_7$  have been studied in great detail [3, 11–14]. The Ru ions are formally  $\text{Ru}^{+4}$  with 4 electrons in the 4d shell that hybridize with the oxygen  $p$  states to form quasi-two-dimensional  $t_{2g}$  bands, with  $d_{xz}$ ,

$d_{yz}$  and  $d_{xy}$  all partially occupied. The Fermi surfaces are well-described by density functional calculations, but there are strong effects of correlation which are revealed by large renormalization of the masses of bands at the Fermi energy [3, 13]. In  $\text{Sr}_3\text{Ru}_2\text{O}_7$  angle-resolved photoemission spectroscopy (ARPES) experiments [3] have revealed shallow renormalized bands with a complex density of states with van Hove singularities near the Fermi level, a situation which is favorable for magnetic instabilities. They are often considered to exemplify the class of materials termed Hund's metals in which there are multiple bands and correlation is due primarily to **intra-atomic** exchange interactions characterized by the Hund's rule coupling which favors high spin configurations [15–17]. The effects depend upon the occupancies of the atomic-like orbitals and lead to correlation on multiple energy scales. The striking effects of correlation were established already in the 1960's for single-impurities with spin  $S$  coupled to a sea of conduction electrons, where the characteristic Kondo temperature decreases exponentially with  $S$  [18–20]. More recently it has been realized that the effects extend to crystals with bandwidth significantly larger than Hund's exchange energies as shown in a number of studies using dynamical mean field theory (DMFT), which is a self-consistent impurity solution. For example, a recent DMFT calculation for  $\text{Sr}_2\text{RuO}_4$  using

realistic parameters from DFT calculations finds a two-stage process of screening orbital and spin fluctuations, so that Fermi-liquid behavior sets in only with spin coherence below  $T_{FL} \sim 25$  K [21].

Triple-layer  $\text{Sr}_4\text{Ru}_3\text{O}_{10}$  exhibits ferromagnetic order below  $T_c \approx 105$  K with a low temperature ( $T$ ) average moment of  $1.1 \mu_B/\text{Ru}$  parallel to the  $c$ -axis that is about half the maximum moment of 2 for  $\text{Ru}^{+4}$  ions populating three energy levels. For weak in-plane fields this magnetic moment rises to a maximum at  $\sim 60$  K and is then suppressed again close to zero at low temperature [5, 22, 23]. The observation of two field-dependent steps for the in-plane metamagnetism in  $\text{Sr}_4\text{Ru}_3\text{O}_{10}$  have prompted speculation about the role of multiple van-Hove singularities near  $E_F$  and/or the inequivalence of the Ru sites in the central versus two outer layers of the tri-layer crystal structure [6]. Subsequent analysis of neutron diffraction data indeed identifies layer-dependent moments and models of layer-dependent spin-orientations are proposed [24–26].

In this work we report spin-resolved ARPES for  $\text{Sr}_4\text{Ru}_3\text{O}_{10}$  which reveals new correlated electron phenomena that are qualitatively different from  $\text{Sr}_2\text{RuO}_4$  and  $\text{Sr}_3\text{Ru}_2\text{O}_7$  due to the ferromagnetic order. The results are in general agreement with recent ARPES experiments [27] and with DFT calculations [28] which found very different occupancies of the  $t_{2g}$  bands. There are wide electron-like minority-spin bands at the Fermi energy that are less than half-filled. The majority spin bands are filled or almost filled with hole-like bands at the Fermi energy; however, present-day functionals are not accurate enough to make a definitive prediction. The present work shows definitively the minority spin conduction bands, and almost filled majority spin bands that form a Fermi liquid with sharp hole-like Fermi surfaces at low temperature. Spin-resolved ARPES reveals narrow bands that are almost completely spin polarized with opposite polarization in different parts of the BZ. Moreover, the two narrow bands have different  $d_{xz/yz}$  orbital origins whose dominant DFT characters reside in different layers of the tri-layer crystal structure. Like  $\text{Sr}_3\text{Ru}_2\text{O}_7$ , narrow bands with large densities of state are a possible mechanism for metamagnetic behavior, and in  $\text{Sr}_4\text{Ru}_3\text{O}_{10}$  the variation of the spin-polarization, with orbital and layer differentiation, provides new possibilities.

In addition, we find a striking temperature dependence of the narrow bands near the Fermi energy. While, the spin-polarization rapidly jumps to  $>60\%$  below  $T_c$ , the spectral weight dramatically increases down to  $<20$  K reminiscent of a Kondo-like effect in previous studies of Hund’s metals [29, 30].

There are several recent papers on related ferromagnetic systems. STM-based quasiparticle-interference measurements of  $\text{Sr}_4\text{Ru}_3\text{O}_{10}$  [31] could not detect the spin polarization directly, but have observed features in agreement with the minority spin Fermi surfaces found

in the present work. The majority spin Fermi surface bands described here were not observed, but a van Hove singularity dispersion was detected with a much smaller energy-scale [32] than the spin-majority saddle-band reported here. A study of films of the three-dimensional  $\text{SrRuO}_3$  that combined DMFT and spin-resolved ARPES [9] found both spin-split itinerant bands crossing  $E_F$ , and a momentum-independent localized spin-majority background at high binding energy as part of a “dual” ferromagnetism characterization.

## Methods

Single crystals of  $\text{Sr}_4\text{Ru}_3\text{O}_{10}$  were grown using flux techniques described in Ref. [33]. Spin-integrated ARPES in the photon energy range of 30-150 eV was performed at the MERLIN beamline 4.0.3 of the Advanced Light Source (ALS) employing both linear horizontal (LH) and linear vertical (LV) polarizations from an elliptically polarized undulator. A Scienta R8000 electron spectrometer was used in combination with a six-axis helium cryostat goniometer in the temperature range of 10-150 K with a total energy resolution of  $\geq 15$  meV and base pressure of  $< 5 \times 10^{-11}$  Torr.

Spin-resolved ARPES was performed at ALS beamline 10.0.1 using 56 eV and 76 eV LH-polarized x-rays. A Scienta-Omicron R4000 DA30 spectrometer with two Ferrum spin detectors [34] was used for data acquisition. Samples were *in-situ* field-cooled from  $>120$  K to 14 K with  $c$ -axis field-alignment prior to cleavage. Only  $c$ -axis spin-asymmetry was measured for this study. More details about the spin-integrated and spin-resolved ARPES measurements are provided in the supplementary material [35].

The ARPES results are compared to predictions of spin-polarized density functional theory (DFT) calculations of the ferromagnetic ground state of  $\text{Sr}_4\text{Ru}_3\text{O}_{10}$  using the pseudopotential, plane-wave implementation of DFT in Quantum Espresso [36, 37] and using the PBEsol exchange-correlation functional [38] without and with spin-orbit coupling as described in Ref. [28]. Additional LDA exchange-correlation functional predictions are provided in the supplementary materials [35].

## Low Temperature Electronic Structure

### *Spin-integrated ARPES*

We first present low temperature constant energy high-symmetry ARPES maps and electronic band dispersions of  $\text{Sr}_4\text{Ru}_3\text{O}_{10}$  in Fig. 1. The layered structure of this material exhibits opposite in-plane  $\text{RuO}_6$  octahedral rotations between the middle and outer layers, as illustrated

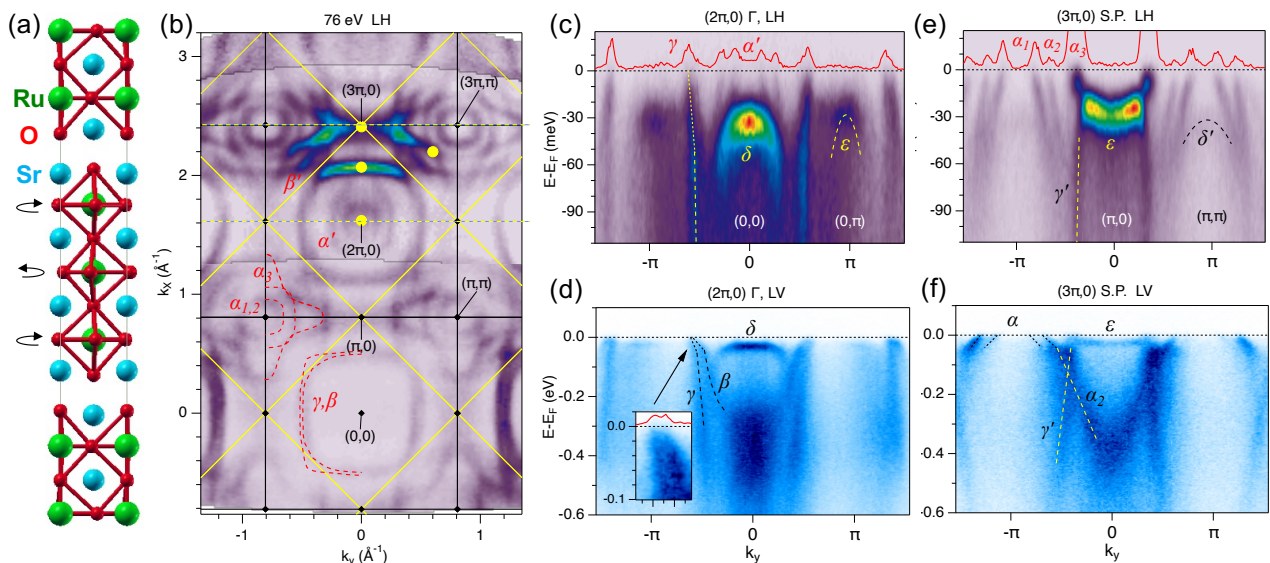


FIG. 1: **Spin-integrated ARPES electronic structure of low temperature  $\text{Sr}_4\text{Ru}_3\text{O}_{10}$ .** (a) Side view of the three-layer crystal structure with oxygen octahedra rotation directions indicated. (b) Fermi surface map at  $h\nu=76$  eV using LH polarization. (c) Near- $E_F$  band dispersion image for the horizontal dotted line in (b) through  $(2\pi,0)$  with labeled band features and  $E_F$ -crossings. (d) Corresponding wider energy band image using LV polarization. Inset shows a zoom of the two near-parallel  $E_F$ -crossing bands. (e, f) Band dispersion images for the horizontal dotted line in (b) through  $(3\pi,0)$ . Dots in (b) indicate where spin-resolved ARPES spectra were measured. Band and FS contour labeling follow  $\text{Sr}_2\text{RuO}_4$  BZ location and  $d$ -orbital origins for  $(\alpha, \beta, \gamma)$  and Ref. [27] for  $(\delta)$ . Zone-folded bands are labeled with a prime ( $'$ ).

in Fig. 1(a), which results in an in-plane doubling of the unit cell and a zone-folding of the (unrotated) tetragonal electronic structure into a smaller  $45^\circ$ -rotated diamond-shaped Brillouin zone (BZ), shown as yellow lines in Fig. 1(b,c). The spectral intensities of the zone-folded bands are observed to be weak in the photon energy range of these ARPES measurements, and so for this study, we use  $(\pi,0)$  zone-edge and  $(\pi,\pi)$  zone-corner tetragonal BZ labeling for discussion of experimental and theory results.

Figure 1(b) shows a spin-integrated FS map spanning two BZs measured using a photon energy of 76 eV with LH polarization. Spin-integrated data were taken using 76 eV photons since a key shallow hole-band ( $\delta$ ) at the  $\Gamma$ -point displayed in Fig. 1(c,d) is greatly enhanced at this photon energy (see Figure S1). Consistent with the previous ARPES study [27], this shallow -30 meV band, exhibits a maximum cross section in the first BZ using LV polarization. Important for our subsequent spin-ARPES measurements, it is also relatively strong in the second BZ using LH polarization, and additionally enhanced at 56 eV, as shown in the supplementary Fig. S1 [35].

A second key high symmetry shallow band in the  $(\pi,0)$  region, whose -30 meV deep electron-like dispersion ( $\varepsilon$ ), shown in Fig. 1(f), is observed to be strongly enhanced at the  $(3\pi,0)$  point between second and third BZs for 76 eV and LH polarization. Similar to  $\text{Sr}_2\text{RuO}_4$ , this tetragonal zone edge feature is actually a saddle-point van Hove singularity, whose orthogonal hole-like dispersion is evident

in Fig. 1(c) at  $(0,\pi)$ .

A prominent feature in the Fermi map in Fig. 1(b) is the larger zone-centered rounded-square FS contour visible in both BZs, and especially enhanced in intensity along one edge in the second zone at  $\sim(2.5\pi,0)$ . This feature is actually composed of two wider-energy electron band dispersions, highlighted by LV photon polarization in Fig. 1(d), with very different band minima. The outer band ( $\gamma$ ) has a light mass dispersion originating from below -0.7 eV, while the inner band ( $\beta$ ) emerges from a high-intensity band minimum at -0.35 eV. As discussed in the previous ARPES study [27], both bands have a heavier mass ‘kink’ dispersion from -40 meV to  $E_F$ , resulting in a near-parallel Fermi velocity and small momentum-separation along  $k_x$  and  $k_y$  [inset in Fig. 1(d)] that becomes larger at the diagonal corners of the FS contour.

Another distinct feature of the low temperature band structure is a pair of concentric small square FS contours ( $\alpha_{1,2}$ ) located inside a flower-shaped FS contour ( $\alpha_3$ ) at the tetragonal  $(\pi,\pi)$  zone corner, mostly clearly visible at  $(3\pi,\pm\pi)$  in Fig. 1(b). They originate from hole-bands, shown in Fig. 1(e) for LH polarization, that are only sharp down to -40 meV and then become broader and less distinct down to -80 meV as they come closer to a strong intensity hole band ( $\gamma'$ ) centered on  $(\pi,0)$  that intercepts the shallow saddle-point electron band ( $\varepsilon$ ). The higher binding energy (BE) dispersion of the outer  $(\pi,\pi)$  hole band ( $\alpha_2$ ), crossing the  $(\pi,0)$  hole band ( $\gamma'$ ) and

reaching -0.4 eV, is visible with LV polarization in Fig. 1(f). Similar to the large FS electron bands ( $\gamma/\beta$ ), the  $(\pi,\pi)$  hole bands ( $\alpha_{1,2}$ ) also have a distinct heavier mass Fermi velocity kink above -40 meV compared to its higher BE dispersion.

The octahedral rotation effect of zone-folding of tetragonal zone bands ( $n$ ) is also visible in the Fig. 1, labeled as ( $n'$ ). The two concentric square  $(\pi,\pi)$  FS contours ( $\alpha$ ) appear with weak intensity ( $\alpha'$ ) at both (0,0) and  $(2\pi,0)$   $\Gamma$  points in Fig. 1(b), and their sharp band dispersions are clearly visible at (0,0) in Fig. 1(d) between the -30 meV hole band and  $E_F$ . The converse zone-folding of the (0,0) flat band ( $\delta$ ) to  $(\pi,\pi)$  is also evident in a faint hole-like spectral intensity ( $\delta'$ ) at -30 meV interior to the distinct hole bands at  $(3\pi,\pm\pi)$  Fig. 1(f) (see also supplementary Fig. S7 [35]). Zone-folding of the large rounded-square zone-centered FS contour ( $\gamma$ ) is also observable ( $\gamma'$ ) in Fig. 1(b), centered at all of the  $(\pm\pi,\pm\pi)$  and  $(3\pi,\pm\pi)$  points. Similarly, the strong intensity light mass band ( $\gamma'$ ) in Fig. 1(e,f) that is hole-like relative to  $(\pi,0)$  and terminates at the saddle-point band ( $\varepsilon$ ), is identified to be the zone-folded replica of the electron-like band ( $\gamma$ ) centered on (0,0).

### Spin-resolved ARPES

We now turn attention to identifying the spin-polarization of different key ARPES features identified by yellow dots in Fig. 1(b). The representative spin-resolved ARPES spectra in Fig. 2, for the  $c$ -axis cleaved crystal, show only the  $c$ -axis vector component of the spin-polarization parallel to the field-cooled magnetization direction along the magnetic easy axis. For the  $\Gamma$ -point flat band spectrum at the  $(2\pi,0)$  hotspot ( $\delta$ ) measured with a photon energy of 56 eV, the narrow -30 meV peak shows a strongly spin-minority polarization (i.e. spin direction opposite to the global magnetic moment) in Fig. 2(a). At higher binding energy, the spectrum shows a sign reversal to spin-majority polarization with uniform 20% amplitude across a broad spectral hump centered at -0.3 eV. While the net minority spin polarization at the narrow band maximum amplitude is evaluated to be only 50%, isolation of the spin-dependent peak amplitudes from modeled background intensities (dashed lines), results in much higher spin-polarizations, as discussed in supplementary section S1 [35].

In contrast, the narrow peak ( $\varepsilon$ ) at the saddle-point  $(3\pi,0)$ , measured at 76 eV, shows a strong spin-majority polarization in Fig. 2(b), opposite to that of the  $\Gamma$ -point narrow band, but with a same-sign  $\sim 30\%$  spin-majority polarization at higher binding energy.

Spin-resolved spectra were also acquired at two other larger band-velocity  $E_F$ -crossing  $k$ -points. The spectra at the large zone-centered rounded-square FS contour ( $\gamma/\beta$ ), measured at  $\approx(2.5\pi,0)$  and 76 eV, shows a dis-

tinct spin-minority composition similar to that of the  $\Gamma$ -point flat band [Fig. 2(c)], and eventual sign-reversal to spin-majority polarization below -0.5 eV. The spectra at the intermediate-sized square FS contour ( $\alpha_2$ ) close to  $(\pi,\pi)$  measured at 56 eV shows a spin-majority polarization similar that of to the nearby  $(3\pi,0)$  narrow band [Fig. 2(d)], but with distinctly weaker spin-polarization. Assuming same-sign spin-polarization along FS contours and ignoring weak intensity zone-folded bands, a pattern of near- $E_F$  states emerges of spin-minority polarization close to the zone-center and spin-majority polarization along the tetragonal zone boundary. In the next section, we will see that this is a general consequence of having bands dispersing upward from the zone center with an exchange splitting nearly as large as the bandwidth.

Finally, in Fig. 2(e), a wide energy range spin-resolved spectrum at the  $(3\pi,0)$  point shows the spin-majority polarization below the near- $E_F$  peak extending uniformly all the way to the top of the oxygen bands, where an opposite spin-minority polarization of two narrow O-band states exists. Notable for later discussion, is that the distinct uniform 20% spin-majority polarization above -2 eV in the Ru- $d$  valence band region does not persist in or below the oxygen band region.

### Comparison with DFT calculations

Together with recent spin-polarized DFT calculations [28], the present experimental results allow us to understand the major features of the electronic states. Like the non-magnetic ruthenates  $\text{Sr}_2\text{RuO}_4$  and  $\text{Sr}_3\text{Ru}_2\text{O}_7$ , which have been studied extensively [13, 14], the bands near the Fermi energy are derived mainly from the Ru  $d$   $t_{2g}$ ,  $d_{xy}$  and  $d_{xz/yz}$  manifold of states mixed with oxygen  $p$  states, but the results are very different due to the trilayer structure and the magnetism. In this section we compare with the DFT calculations using the PBEsol functional reported in [28]. Similarities and differences using other functionals are discussed in the supplementary material.

In all cases, the dispersion of the bands in the plane starts at the zone center (0,0) and rise steeply to a maximum at  $(\pi,\pi)$  with a saddle-point at  $(\pi,0)$  which leads to a large density of states (DOS). The  $d_{xy}$  bands disperse in both directions, and the  $d_{xz/yz}$  bands have one dimensional character, each dispersing strongly in one direction and nearly flat in the other. In  $\text{Sr}_4\text{Ru}_3\text{O}_{10}$  the three planes of Ru and oxygen atoms are strongly coupled to form bonding (B), non-bonding (NB) and antibonding (AB)  $d_{xz/yz}$  bands. This is analogous to the bonding and antibonding bands of the two-layer material  $\text{Sr}_3\text{Ru}_2\text{O}_7$ ; but there is a important difference because the central layer is not equivalent to the outer two layers, whereas the two layers are equivalent in  $\text{Sr}_3\text{Ru}_2\text{O}_7$ .

The rotations of the oxygen octahedra double the unit

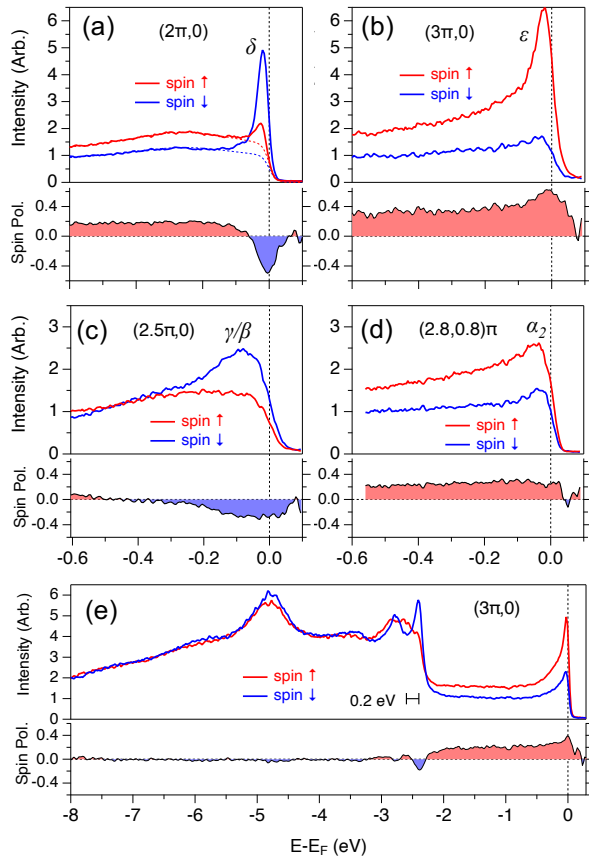


FIG. 2: **Spin-resolved ARPES at low temperature.** Spin-up and spin-down spectra measured at 14 K and the net spin-polarization (Spin Pol.) at four selected  $k$ -locations: (a) the  $(2\pi,0)$   $\Gamma$ -point, (b) the  $(3\pi,0)$  saddle-point region, (c) the large FS contour centered on  $(2\pi,0)$ , and (d) a square hole FS contour centered on  $(3\pi,\pi)$ . The four  $k$ -points are identified as yellow dots in Fig. 1. All measurements use LH polarization excitation and are overall scaled to unity at high binding energy for the weaker intensity spin-minority background. (e) Wide spectrum at  $(3\pi,0)$  showing uniform spin-majority background in the Ru-d valence band region and spin-minority narrow peaks at the top of the oxygen bands.

cell leading to the smaller Brillouin zone as shown in Fig. 1, the same as in  $\text{Sr}_3\text{Ru}_2\text{O}_7$ , which also has rotated octahedra and a cell that is doubled in the same way. However, as illustrated in Fig. 1, there are only weak effects in the observed intensities and the data can be analyzed in an extended range of  $k$ -space corresponding to the larger tetragonal Brillouin zone, with weak replicas due to the doubling of the cell. This is indicated in Fig. 3(a) where the bands from [28] are “unfolded” schematically to show the regions of  $k$ -space where the intensity is large with weak replicas indicated by light lines.

The qualitative difference in  $\text{Sr}_4\text{Ru}_3\text{O}_{10}$  is the ferromagnetism which leads to splitting of the bands into minority- and majority-spin bands. Since there is a large

moment, the majority-spin bands have large occupation so that the Fermi energy is near the top of the bands. In contrast, the minority-spin bands have reduced occupation and the Fermi energy is in the lower part of the bands. As shown in Fig. 3(a), the wide electron-like minority-spin bands dispersing steeply upward from  $(0,0)$  and crossing the Fermi energy. These can be identified with the experimental bands that disperse upward in Fig. 1(d) and form the square-shaped Fermi surface that fills most of the BZ in Fig. 1(b), and are found to be minority spin in Fig. 2(c). This is a robust result of the theory that depends only on characteristic shapes of the  $d_{xy}$  and  $d_{xz/yz}$  bands, and the ferromagnetic order.

The prediction that the majority-spin bands are full or nearly full is also a robust result of the DFT calculations, and since the effects of band folding are small, we expect strong intensity in ARPES measurements in the region around  $(\pi,\pi)$ . This provides an interpretation for the majority-spin bands observed in the experiment; however, the degree of filling depends on the energy difference between the majority and minority-spin bands and effects of correlation. As discussed below, present-day theory is not at the point where the energies can be predicted with accuracy of a few tenths of an eV, and we will use the experimental measurements as a guide.

There are two other definite predictions of the theory that provide the basis for understanding the spin-polarized narrow bands near the Fermi energy around  $(0,0)$  and  $(\pi,0)$  which are observed in the experiments. The first point is that the only states with large intensity near  $(0,0)$  are spin-minority bands; as indicated in Fig. 3(a), the spin-majority bands with large intensity near  $(0,0)$  are well below the Fermi energy and any majority spin bands are due to the weak effects of folding. Thus, even though there are several minority-spin bands in this region, with uncertainties in the theory and the fact that energies are affected by correlation beyond the DFT calculations, nevertheless, it is clear that the narrow peak observed in the experiment should be derived from bands that are overwhelmingly minority spin, as observed in the experiment. The second conclusion from the calculations relates to the states near the saddle point  $(\pi,0)$ . As is clear from Fig. 3(a), the theoretical calculation finds majority spin bands in this region below the Fermi energy, the same bands that form the majority-spin Fermi surfaces around  $(\pi,\pi)$ . We can expect that the narrow peak observed just below the Fermi energy observed in the experiments is formed primarily from these bands, in agreement with the majority spin-polarization found in the experimental results.

A more quantitative analysis of the experimental results provides more information that helps to narrow down the uncertainties in the theory, and we have analyzed the comparison with the calculations in more detail. Comparison with the DFT calculations provides a consistent interpretation of the experimental results for the

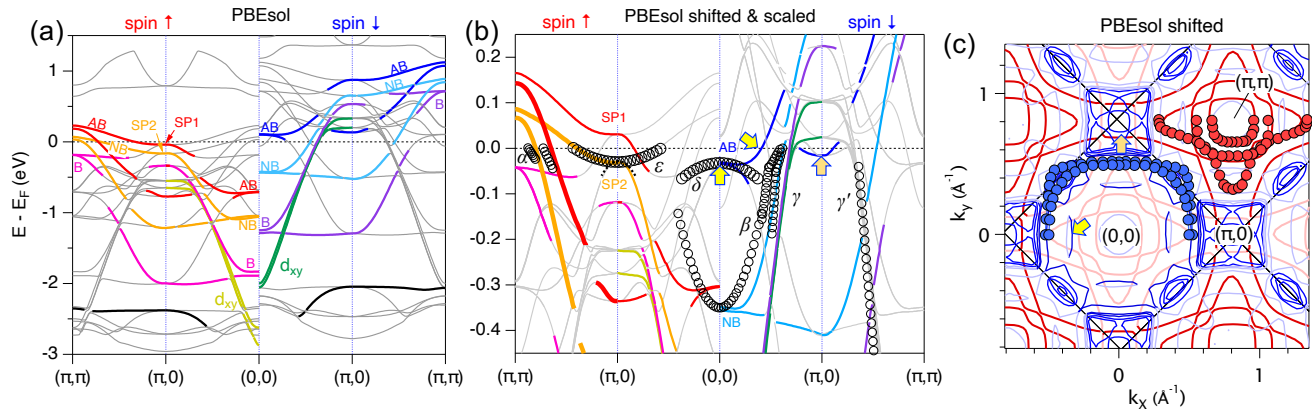


FIG. 3: **Spin-resolved DFT and comparison to ARPES.** (a) DFT GGA-PBEsol theory calculation of spin-up/down band structure with  $\approx 0.9$  eV exchange splitting, resulting in the  $(0,0)$  AB band just above  $E_F$  and the  $(\pi,0)$  saddle-point band SP1 crossing below  $E_F$ . (b) Energy-shifted and scaled PBEsol bands with  $\approx 0.6$  eV exchange splitting, resulting in the  $(0,0)$  AB band below  $E_F$ , and the  $(\pi,0)$  SP2 band crossing below  $E_F$ . Energy scale renormalization by  $\approx 2\times$  then provides good agreement to experimental bands (open circles). (c) Comparison of experimental FS contours (filled circles) to PBEsol contours including the energy shifts in (b). Solid colored lines emphasize the tetragonal band or contour origin, while lighter gray lines correspond to features with octahedral-rotation and zone-folding origins. Arrows in (b) and (c) indicate two key disagreements that are resolved with the inclusion of spin-orbit coupling [35].

narrow bands near  $(0,0)$  and  $(\pi,0)$  and the Fermi surfaces around  $(\pi,\pi)$ , as long as we allow for small shifts of the calculated bands and renormalization of DFT band energies close to  $E_F$ , similar to the other Sr ruthenates. Fig. 3(b) show the bands near the Fermi energy, with ARPES bands (open circles) compared to the PBEsol calculation with  $-0.16$  eV ( $+0.10$  eV) energy-shift corrections to the minority (majority) spin bands, and a  $2\times$  energy scale renormalization which then provides good agreement to the heavy effective mass dispersions of both the  $(0,0)$  hole and  $(\pi,0)$  electron narrow bands. The effect of the downward shift of the energy on the minority-spin bands is to move the band at  $\Gamma$  from just above  $E_F$  in the DFT calculation shown in Fig. 3(a) to just below as shown in Fig. 3(b); together with the renormalization, this provides an explanation for the narrow band ( $\delta$ ) at  $\Gamma$  shown in Figs. 1(c) and 1(d) and in Fig. 2(a), and represented by the line of circles near  $(0,0)$  in Fig. 3(b). The effect of the upward shift of the majority-spin bands is to move the AB state at  $(\pi,0)$  labeled SP1 in Fig. 3(a) to above  $E_F$  and the state labeled SP2 to just below  $E_F$ , where it provides an explanation for the observed majority-spin band at  $-30$  meV labeled  $\varepsilon$  in Figs. 1(e) and 2(b). The shift leads to better agreement with experiment, which finds only one band below  $E_F$  at  $(\pi,0)$  in this energy range, and it also improves the agreement for the majority-spin bands (shown as the lines of circles) that cross the Fermi energy along the direction  $(\pi,0)$  to  $(\pi,\pi)$ . The Fermi surfaces for the shifted bands are shown in Fig. 3(c), which shows good overall agreement with the major features of the experimental results.

However, the shifts of the bands do lead to two major

discrepancies with experiment, highlighted by arrows in Fig. 3(b) and (c). First, the PBEsol calculations predict a two-fold band degeneracy just below  $E_F$  at  $(0,0)$ , which results in the prediction of both downwards and upwards dispersing AB branches, and an electron-like  $E_F$ -crossing which is not observed experimentally. Second, the downward shift leads to spin-minority bands at  $E_F$  in a region around  $(\pi,0)$  for most combinations of energy-shift and energy-scaling corrections. These effects lead to bands and pieces of Fermi surface marked by arrows in Figs. 3(b) and 3(c), which are not observed in the experiments.

The inclusion of spin-orbit coupling provides a resolution of these discrepancies, as described in detail in the supplementary information. In Fig. S4(a) is shown the bands including spin-orbit coupling from [28], shifted and scaled in a way corresponding to that of Fig. 3(b). Since the spin-orbit coupling mixes the spins it is not a simple matter to identify the majority and minority spin projections and to shift the bands independently, and the bands in Fig. S4 are derived by approximations described there. It turns out that the effects are not large overall, but there are major consequences for states near the Fermi energy. One is that the degeneracy of the AB states is lifted so that the upward curving band at  $\Gamma$  is above the Fermi energy, consistent with experiment that did not observe such a band. The other discrepancy is a quantitative matter and it turns out that spin-orbit coupling raises the energy of the minority-spin bands at  $(\pi,0)$  to above the Fermi energy. The resulting Fermi surfaces, shown in Figs. S4(b) and S4(c), are in quantitatively better agreement with experiment, with the absence of the FS contours marked by arrows in Fig. 3(c).

The shifts of the majority-spin bands upward and the minority-spin downward relative to the Fermi energy has the effect of reducing the differences between both the energies and the occupations of the majority and minority bands. The average energy difference, called the exchange energy, is a consequence of interactions which are taken into account in approximate ways depending on the functional used in the calculation. The shifts of the bands calculated using the PBEsol functional amount to a reduction of the exchange splitting from  $\sim 0.9$  eV to about  $\sim 0.6$  eV. This results in a smaller spin moment and provides a possible explanation for the discrepancy between PBEsol prediction of a  $1.77 \mu_B$  average moment per Ru site [28] and the significantly smaller experimental value of  $1.1 \mu_B/\text{Ru}$  [5].

A spin-polarized DFT calculation using the LDA exchange-correlation functional, shown in the supplementary materials [35], finds a reduced average moment of  $1.36 \mu_B$  and a corresponding reduced exchange splitting of  $\sim 0.6$  eV which is a closer match to the experimental ARPES. A comparison of DFT predictions using LDA, PBEsol, and PBEsol+U functionals is provided in the supplementary materials [35]. The better agreement of the LDA functional to experiment in  $\text{Sr}_4\text{Ru}_3\text{O}_{10}$ , the systematic trend towards increasing exchange splitting and larger moments for  $\text{LDA} \rightarrow \text{PBEsol} \rightarrow \text{PBE96} \rightarrow \text{DFT+U}$ , and the prediction of a large moment half-metal groundstate (not observed) for small U is consistent with previous comparative studies of DFT exchange-correlation functionals for magnetism in  $\text{SrRuO}_3$  [39],  $\text{Sr}_3\text{Ru}_2\text{O}_7$  [40] and ferromagnetic transition metals [41].

### Narrow band T-dependence

We next turn our attention to the temperature dependent amplitude and spin-polarization of the prominent narrow bands at  $-30$  meV. Figures 4(a) and (b) present the fine temperature-step spin-integrated evolutions of the narrow band amplitudes. Both narrow bands exhibit dramatic amplitude reductions towards higher temperature and  $T_c$ , with approximately linear dependence as shown in Fig. 4(c).

The spin-resolved temperature evolution of the  $\Gamma$ -point was also measured at the  $56$  eV  $(2\pi, 0)$   $k$ -location with spectra presented in Fig. 4(d) for  $\approx 30\text{K}$  steps from  $14\text{K}$  to  $120\text{K}$ , along with their spin-polarization energy profiles. The strong spin-minority narrow band amplitude is observed to linearly decrease with temperature, consistent with the spin-integrated measurement, whereupon, as expected, the spin-polarization of both the peak and high BE background go to zero above  $T_c$ . The high BE spin-polarization, averaged over the energy interval of  $-0.2$  to  $-0.6$  eV, exhibits a weak monotonic decline from  $21\%$  to  $15\%$  at  $T_c$  as summarized in Fig. 4(e). with comparison to a bulk magnetization curve [7] that

exhibits a similar weak decline. In contrast, the raw spin-polarization analysis of the narrow peak exhibits a steady linear decline, seemingly correlated to the linear amplitude variation. However, with consideration of a background subtraction to isolate the spin-asymmetry of the narrow peak, and also with a second BZ large angle  $1/\cos\theta$  correction factor of  $1.11$  [see supplemental Fig. S2 for more details], a modified  $T$ -dependent spin-polarization profile of the narrow peak in Fig. 4(f) also exhibits a weak decline from  $80\%$  at low  $T$  to  $60\%$  close to  $T_c$ , that scales very well with that of the high BE spin-polarization profile.

### Discussion

We now discuss the implications of our data for the general character of the correlations and the magnetism of  $\text{Sr}_4\text{Ru}_3\text{O}_{10}$ . The traditional simplified pictures are the Stoner model of itinerant band ferromagnetism and, at the other extreme, localized spins which are ordered in the ferromagnetic phase. In the Stoner picture there are well-defined bands and the energy difference between the bands for the two spin states, called the exchange energy, which decreases with temperature until the bands become degenerate above the transition temperature  $T_c$ . On the other hand, the picture of localized spins is that they persist at all temperatures and become disordered above  $T_c$ . The energies of the states remain the same even if the directions of the moments are disordered with no preferred direction. In addition, at all temperatures one expects localized states to lead to broadening of band-like features, so that the spectra would not show sharp features with dispersion as a function of momentum. In a Fermi-liquid metal, however, there is another important consideration. No matter what is the nature of the states, at low temperature there should be a sharp Fermi surface satisfying the Luttinger theorem. Additionally, for the two ferromagnetic ruthenates  $\text{SrRuO}_3$  and  $\text{Sr}_4\text{Ru}_3\text{O}_{10}$ , the magnetization should be given by the difference in the volumes of the Fermi surfaces for the two spin states multiplied by  $\mu_B$ . See the supplemental sections S4 and S5 for more on the effects of spin orbit coupling, and comparison and contrast of the two ferromagnets.

The experimental data presented here for  $\text{Sr}_4\text{Ru}_3\text{O}_{10}$  in Figs. 1 and 2 shows clearly Fermi surfaces for both spins, neither of which act as completely localized. To assess localization we must turn to measurements as a function of energy (away from  $E_F$ ), at low temperature, e.g. incoherent broadening, and/or the behavior as a function of temperature. As is also true for  $\text{SrRuO}_3$ , away from  $E_F$ , the spectra show no overt spectroscopic signatures of localization, such as split-off Hubbard bands or atomic multiplets, so we must focus on T-dependences and strong incoherent broadenings as the important signatures of local moments. Based on analysis of such

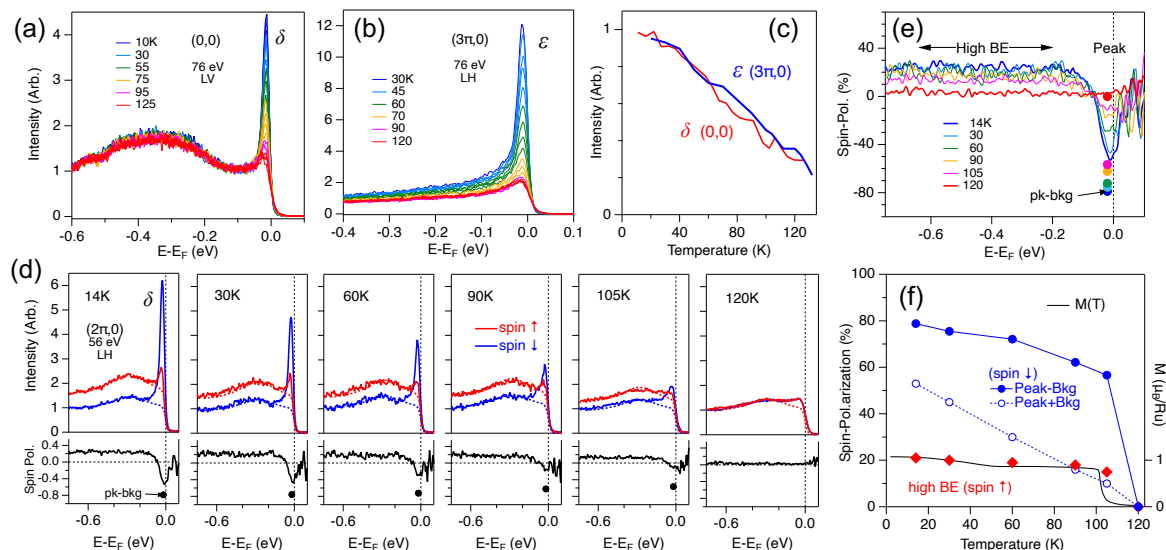


FIG. 4: **Narrow band temperature dependent spin-polarization.** Spin-integrated spectra at (a) the (0,0)  $\Gamma$ -point and (b) the  $(3\pi,0)$  saddle-point exhibiting dramatic temperature dependent amplitude reductions of the strong narrow peaks warming to above  $T_c$ . (c) Linear behavior of the temperature evolution of the two narrow peak amplitudes. (d) Spin-polarized  $(2\pi,0)$   $\Gamma$ -point spectra and spin-polarization profiles for selected temperatures from 14-120K. (e) Comparison of the spin-polarization profiles from (d). (f) Summary of the spin-polarization of the average of the high binding energy region shown in (e), the narrow peak amplitude, and the background-subtracted narrow peak spin-polarization corresponding to the dots in (d) and (e), including an additional  $1.11\times$  geometry-correction. A  $c$ -axis bulk magnetization profile  $\text{Sr}_4\text{Ru}_3\text{O}_{10}$  is provided for reference.

signatures, a “dual ferromagnetism” model has recently been proposed for  $\text{SrRuO}_3$ [9], in which the moments of the spin-minority electrons are itinerant and the moments of the spin-majority electrons are localized.

In a general way,  $\text{Sr}_4\text{Ru}_3\text{O}_{10}$  also manifests such a duality, but it is more complex and nuanced than in the neatly binary picture proposed for  $\text{SrRuO}_3$ . In another publication we will present the detailed ARPES  $T$ -dependence and explore this complexity, along with how it might fit into a Hund’s metal picture. Here we only summarize. We begin by noting a low- $T$  similarity to  $\text{SrRuO}_3$  and its spin polarized DMFT calculation [9], that the low- $T$  Ru- $d$  valence band region above -2 eV is broad and incoherent, implying some localization, and shows a uniform 20% spin-majority polarization in Fig.2(e). We attribute the polarization to a net larger spin-majority DOS rather than an extrinsic inelastic background due to spin-dependent mean free paths [42], which would persist below the oxygen bands. For the  $T$ -dependence, a broad general characterization is that (a) at  $T_c$  the up and down spin spectra remain totally different, a clear failure of the Stoner model, (b) the large rounded-square Fermi surface(s), identified as minority spin, survive with minimal broadening above  $T_c$ , (as measured by spin-integrated ARPES, not shown), even though there is no macroscopic average magnetization, whereas (c) the small hole-like Fermi surfaces for

the majority spins broaden with temperature until they are only barely discernible for  $T > T_c$ . Of the limited  $T$ -dependent data actually reported here, we take note that both the spin majority and spin-minority narrow band peaks shown in Fig. 4 have  $T$ -independent energies, suggesting a  $T$ -independent exchange splitting for both. However the spin-majority hole bands ( $\alpha_{1,2}$ ) that cross  $E_F$  at  $(\pi,\pi)$  do have momentum and energy shifts with increasing  $T$ , signaling some decrease of exchange splitting, although well short of actual collapse at  $T_c$ .

Our experiments also show more aspects to magnetic behavior in  $\text{Sr}_4\text{Ru}_3\text{O}_{10}$ . The dramatic  $T$ -dependences of the narrow band amplitudes in Fig. 4 are strongly reminiscent of  $f$ -electron local-moment Kondo lattice coherence evolutions. Such a  $T$ -dependence is consistent with key signatures of correlated Hund’s metal behavior, for which a two-stage screening process of orbital and spin-fluctuation coherence has been proposed [21]. In addition, the two experimental spin-minority  $E_F$ -crossing bands, as well as the two spin-majority hole bands at  $(\pi,\pi)$ , exhibit additional heavier mass kinks in their dispersion, which reflect additional energy correlations and/or electron-lattice coupling not included in the DFT calculations. Correlation of the kink energy scales in  $\text{SrRuO}_3$  [43] and in  $\text{Sr}_4\text{Ru}_3\text{O}_{10}$  [27] to Raman spectroscopy vibrational modes have suggested an electron-boson coupling origin. On the other hand, DFT+DMFT

calculations with Hund's coupling ( $U=2.3$  eV,  $J=0.4$  eV) find rounded band velocity renormalizations for  $\text{Sr}_2\text{RuO}_4$  [13] and orbital-dependent heavier dispersion anomalies confined to  $\pm 0.1$  eV about  $E_F$  in  $\text{SrRuO}_3$  [9], suggestive of Hund's-assisted electronic correlation origins.

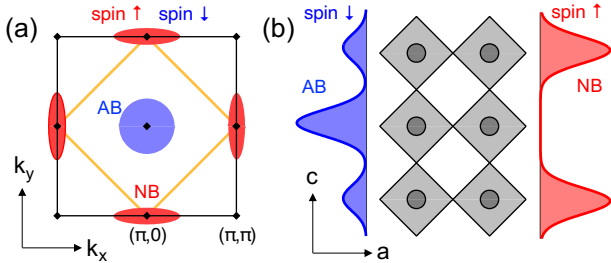


FIG. 5: **Summary of low temperature  $\text{Sr}_4\text{Ru}_3\text{O}_{10}$  spin-polarized narrow bands.** (a) Momentum-space schematic of the highly coherent -30 meV narrow spin-majority saddle-bands at  $(\pi,0)$  and spin-minority hole-band at  $(0,0)$ . Zone-folding effects are not represented. (b) Schematic of the spatial distribution of the narrow band weights in the outer and central layer of the tri-layer structure.

Next, we discuss the narrow band spin-polarization in relation to the magnetic behavior specific to the trilayer structure of  $\text{Sr}_4\text{Ru}_3\text{O}_{10}$ . Layer-dependent moments have been identified from polarized neutron diffraction analysis, and models of layer-dependent spin-orientations have been proposed for the in-plane metamagnetic behavior [24–26]. Similar to a model of in-plane moments with antiferromagnetic coupling between adjacent outer Ru layers [26], the application of modest pressure to  $\text{Sr}_4\text{Ru}_3\text{O}_{10}$  reveals an instability of the  $c$ -axis ferromagnetic state, by inducing a transition to an antiferromagnetic state with the magnetic easy axis aligned within the basal plane [7]. Here, in this  $c$ -axis magnetization ARPES study, we have identified two distinct high-DOS narrow band states below  $E_F$  with large momentum-separation and opposite spin-polarization, as schematically shown Fig. 5(a), which also possess different AB versus NB  $d_{xz/yz}$  orbital origins from the comparison to DFT. The NB orbital has an odd symmetry relative to the central layer mirror plane, and thus contains zero central layer character, while the B and AB orbitals have even symmetry and contain mixed layer character, but with a more dominant central layer spatial origin. Hence, the high-DOS spin-minority narrow band at  $(0,0)$  with AB band origin is spatially localized primarily in the central layer, while the high DOS spin-majority saddle-point van Hove singularity at  $(\pi,0)$  with NB band origin is primarily localized in the outer layers, as schematically represented in Fig. 5(b). A quantitative character breakdown is to be presented elsewhere.

## Summary

This work shows that  $\text{Sr}_4\text{Ru}_3\text{O}_{10}$  displays a remarkable range of spin-polarized features that are important for the understanding of the magnetic behavior. At low temperature: (i) Distinct Fermi surfaces with opposite spin-polarization are found at the zone center and the zone corner, with weak intensity oxygen-octahedron zone-folding effects. (ii) Two separate very high intensity narrow bands exist 30 meV below the Fermi-level, a hole-like band located at the zone-center and a van Hove singularity saddle-band dispersion at the zone boundary, also exhibit opposite nearly-pure spin-polarization. (iii) An intrinsic incoherent spin-majority background exists over the entire Ru- $d$  valence band region. (iv) Sharp spin-minority oxygen bands exist at the top of the oxygen manifold.

The narrow bands exhibit dramatic temperature-dependent amplitude suppression upon warming to  $T_c$ , which we attribute to Hund's metal coherence-like behavior [15–17]. The spin-resolved  $T$ -dependence of the zone center narrow band and the incoherent spin-majority background, shows that both maintain a strong spin-polarization right up to  $T_c$ , similar to the bulk magnetization profile. The  $T$ -independence of the narrow band energies suggests the localized behavior of a constant exchange energy up to  $T_c$  and clear departure from the predictions of simple itinerant ferromagnetism.

Comparison of the sharp low  $T$  FS contours and narrow band energies to spin-polarized DFT calculations, allows quantitative evaluation of the predictions of different exchange-correlation functionals, and identifies the zone center and zone boundary narrow bands to have different anti-bonding versus non-bonding  $d_{xz/yz}$  orbital origins, which in turn have weight predominantly in different layers of the three-layer structure. The strong coherence-like  $T$ -dependence, opposite spin-polarization, momentum separation, and layer-specific localization of the narrow band states are key new ingredients to be considered for the modeling of magnetic and metamagnetic behaviors in  $\text{Sr}_4\text{Ru}_3\text{O}_{10}$ .

## Acknowledgements

Research used resources of the Advanced Light Source, which is a US Department of Energy, Office of Science User Facility under contract no. DE-AC02-05CH11231. This work was supported by the 2019 Innovation Fund of the American Physical Society through the U.S.-Africa Initiative in Electronic Structure. We gratefully acknowledge the African School for Electronic Structure Methods and Applications (ASESMA) and the Abdus Salam International Centre for Theoretical Physics without which this work would not have been done. This work used the

Centre for High-Performance Computing (CHPC), South Africa. GC acknowledges NSF support via grant DMR-2204811.

\* [pngabonziza@lsu.edu](mailto:pngabonziza@lsu.edu)

† [jddenlinger@lbl.gov](mailto:jddenlinger@lbl.gov)

- [1] Y. Maeno, H. Hashimoto, K. Yoshida, S. Nishizaki, T. Fujita, J. G. Bednorz, and F. Lichtenberg, Superconductivity in a layered perovskite without copper, *Nature* **372**, 532 (1994).
- [2] A. Putatunda, G. Qin, W. Ren, and D. J. Singh, Competing magnetic orders in quantum critical  $\text{Sr}_3\text{Ru}_2\text{O}_7$ , *Phys. Rev. B* **102**, 014442 (2020).
- [3] A. Tamai, M. P. Allan, J. F. Mercure, W. Meevasana, R. Dunkel, D. H. Lu, R. S. Perry, A. P. Mackenzie, D. J. Singh, Z.-X. Shen, and F. Baumberger, Fermi surface and van hove singularities in the itinerant metamagnet  $\text{Sr}_3\text{Ru}_2\text{O}_7$ , *Phys. Rev. Lett.* **101**, 026407 (2008).
- [4] M. K. Crawford, R. L. Harlow, W. Marshall, Z. Li, G. Cao, R. L. Lindstrom, Q. Huang, and J. W. Lynn, Structure and magnetism of single crystal  $\text{Sr}_4\text{Ru}_3\text{O}_{10}$ : A ferromagnetic triple-layer ruthenate, *Phys. Rev. B* **65**, 214412 (2002).
- [5] G. Cao, L. Balicas, W. H. Song, Y. P. Sun, Y. Xin, V. A. Bondarenko, J. W. Brill, S. Parkin, and X. N. Lin, Competing ground states in triple-layered  $\text{Sr}_4\text{Ru}_3\text{O}_{10}$ : Verging on itinerant ferromagnetism with critical fluctuations, *Phys. Rev. B* **68**, 174409 (2003).
- [6] E. Carleschi, B. P. Doyle, R. Fittipaldi, V. Granata, A. M. Strydom, M. Cuoco, and A. Vecchione, Double metamagnetic transition in  $\text{Sr}_4\text{Ru}_3\text{O}_{10}$ , *Phys. Rev. B* **90**, 205120 (2014).
- [7] H. Zheng, W. H. Song, J. Terzic, H. D. Zhao, Y. Zhang, Y. F. Ni, L. E. DeLong, P. Schlottmann, and G. Cao, Observation of a pressure-induced transition from interlayer ferromagnetism to intralayer antiferromagnetism in  $\text{Sr}_4\text{Ru}_3\text{O}_{10}$ , *Phys. Rev. B* **98**, 064418 (2018).
- [8] G. Koster, L. Klein, W. Siemons, G. Rijnders, J. S. Dodge, C.-B. Eom, D. H. A. Blank, and M. R. Beasley, Structure, physical properties, and applications of  $\text{SrRuO}_3$  thin films, *Rev. Mod. Phys.* **84**, 253 (2012).
- [9] S. Hahn, B. Sohn, M. Kim, J. R. Kim, S. Huh, Y. Kim, W. Kyung, M. Kim, D. Kim, Y. Kim, T. W. Noh, J. H. Shim, and C. Kim, Observation of spin-dependent dual ferromagnetism in perovskite ruthenates, *Phys. Rev. Lett.* **127**, 256401 (2021).
- [10] M. Malvestuto, E. Carleschi, R. Fittipaldi, E. Gorelov, E. Pavarini, M. Cuoco, Y. Maeno, F. Parmigiani, and A. Vecchione, Electronic structure trends in the  $\text{Sr}_{n+1}\text{Ru}_n\text{O}_{3n+1}$  family ( $n = 1, 2, 3$ ), *Phys. Rev. B* **83**, 165121 (2011).
- [11] A. Damascelli, D. H. Lu, K. M. Shen, N. P. Armitage, F. Ronning, D. L. Feng, C. Kim, Z.-X. Shen, T. Kimura, Y. Tokura, Z. Q. Mao, and Y. Maeno, Fermi surface, surface states, and surface reconstruction in  $\text{Sr}_2\text{RuO}_4$ , *Phys. Rev. Lett.* **85**, 5194 (2000).
- [12] N. J. C. Ingle, K. M. Shen, F. Baumberger, W. Meevasana, D. H. Lu, Z.-X. Shen, A. Damascelli, S. Nakatsuji, Z. Q. Mao, Y. Maeno, T. Kimura, and Y. Tokura, Quantitative analysis of  $\text{Sr}_2\text{RuO}_4$  angle-resolved photoemission spectra: Many-body interactions in a model Fermi liquid, *Phys. Rev. B* **72**, 205114 (2005).
- [13] A. Tamai, M. Zingl, E. Rozbicki, E. Cappelli, S. Riccò, A. de la Torre, S. M. Walker, F. Bruno, P. King, W. Meevasana, M. Shi, M. Radović, N. Plumb, A. Gibbs, A. Mackenzie, C. Berthod, H. Strand, M. Kim, A. Georges, and F. Baumberger, High-resolution photoemission on  $\text{Sr}_2\text{RuO}_4$  reveals correlation-enhanced effective spin-orbit coupling and dominantly local self-energies, *Phys. Rev. X* **9**, 021048 (2019).
- [14] M. P. Allan, A. Tamai, E. Rozbicki, M. H. Fischer, J. Voss, P. D. C. King, W. Meevasana, S. Thirupathiah, E. Rienks, J. Fink, D. A. Tennant, R. S. Perry, J. F. Mercure, M. A. Wang, J. Lee, C. J. Fennie, E.-A. Kim, M. J. Lawler, K. M. Shen, A. P. Mackenzie, Z.-X. Shen, and F. Baumberger, Formation of heavy d-electron quasiparticles in  $\text{Sr}_3\text{Ru}_2\text{O}_7$ , *New J. Phys.* **15**, 063029 (2013).
- [15] A. Georges, L. de' Medici, and J. Mravlje, Strong correlations from Hund's coupling, *Annu. Rev. Condens. Matter Phys.* **4**, 137 (2013).
- [16] L. de' Medici, J. Mravlje, and A. Georges, Janus-faced influence of Hund's rule coupling in strongly correlated materials, *Phys. Rev. Lett.* **107**, 256401 (2011).
- [17] X. Deng, K. M. Stadler, K. Haule, A. Weichselbaum, J. von Delft, and G. Kotliar, Signatures of Mottness and Hundness in archetypal correlated metals, *Nat. Commun.* **10**, 2721 (2019).
- [18] J. R. Schrieffer, The Kondo effect—the link between magnetic and nonmagnetic impurities in metals?, *J. Appl. Phys.* **38**, 1143 (1967).
- [19] A. Blandin, Magnetic impurities in metals, *J. Appl. Phys.* **39**, 1285 (1968).
- [20] C. Jayaprakash, H. R. Krishna-murthy, and J. W. Wilkins, Two-impurity kondo problem, *Phys. Rev. Lett.* **47**, 737 (1981).
- [21] F. B. Kugler, M. Zingl, H. U. Strand, S.-S. B. Lee, J. von Delft, and A. Georges, Strongly correlated materials from a numerical renormalization group perspective: How the Fermi-liquid state of  $\text{Sr}_2\text{RuO}_4$  emerges, *Phys. Rev. Lett.* **124**, 016401 (2020).
- [22] Z. Q. Mao, M. Zhou, J. Hooper, V. Golub, and C. J. O'Connor, Phase separation in the itinerant metamagnetic transition of  $\text{Sr}_4\text{Ru}_3\text{O}_{10}$ , *Phys. Rev. Lett.* **96**, 077205 (2006).
- [23] Z. Xu, X. Xu, R. S. Freitas, Z. Long, M. Zhou, D. Fobes, M. Fang, P. Schiffer, Z. Mao, and Y. Liu, Magnetic, electrical transport, and thermoelectric properties of  $\text{Sr}_4\text{Ru}_3\text{O}_{10}$ : Evidence for a field-induced electronic phase transition at low temperatures, *Phys. Rev. B* **76**, 094405 (2007).
- [24] V. Granata, L. Capogna, F. Forte, M.-B. Lepetit, R. Fittipaldi, A. Stunault, M. Cuoco, and A. Vecchione, Spin-orbital nature of the high-field magnetic state in the  $\text{Sr}_4\text{Ru}_3\text{O}_{10}$ , *Phys. Rev. B* **93**, 115128 (2016).
- [25] F. Forte, L. Capogna, V. Granata, R. Fittipaldi, A. Vecchione, and M. Cuoco, Suppression of the orbital magnetic moment driven by electronic correlations in  $\text{Sr}_4\text{Ru}_3\text{O}_{10}$ , *Phys. Rev. B* **100**, 104440 (2019).
- [26] L. Capogna, V. Granata, B. Ouladdiaf, J. Rodriguez-Velamazán, R. Fittipaldi, and A. Vecchione, Layer dependent antiferromagnetism in the  $\text{Sr}_4\text{Ru}_3\text{O}_{10}$  ruthenate at the metamagnetic-like transition, *J. Magn. Magn. Mater.* **493**, 165698 (2020).
- [27] P. Ngabonziza, E. Carleschi, V. Zabolotnyy, A. Taleb-

- Ibrahimi, F. Bertran, R. Fittipaldi, V. Granata, M. Cuoco, A. Vecchione, and B. P. Doyle, Fermi surface and kink structures in  $\text{Sr}_4\text{Ru}_3\text{O}_{10}$  revealed by synchrotron-based ARPES, *Sci. Rep.* **10**, 21062 (2020).
- [28] G. Gebreyesus, P. Ngabonziza, J. Nagura, N. Seriani, O. Akin-Ojo, and R. M. Martin, Electronic structure and magnetism of the triple-layered ruthenate  $\text{Sr}_4\text{Ru}_3\text{O}_{10}$ , *Phys. Rev. B* **105**, 165119 (2022).
- [29] J. Mravlje, M. Aichhorn, T. Miyake, K. Haule, G. Kotliar, and A. Georges, Coherence-incoherence crossover and the mass-renormalization puzzles in  $\text{Sr}_2\text{RuO}_4$ , *Phys. Rev. Lett.* **106**, 096401 (2011).
- [30] T. Kondo, M. Ochi, M. Nakayama, H. Taniguchi, S. Akebi, K. Kuroda, M. Arita, S. Sakai, H. Namatame, M. Taniguchi, Y. Maeno, R. Arita, and S. Shin, Orbital-dependent band narrowing revealed in an extremely correlated Hund's metal emerging on the topmost layer of  $\text{Sr}_2\text{RuO}_4$ , *Phys. Rev. Lett.* **117**, 247001 (2016).
- [31] I. Benedičič, M. Naritsuka, L. C. Rhodes, C. Trainer, Y. Nanao, A. B. Naden, R. Fittipaldi, V. Granata, M. Lettieri, A. Vecchione, and P. Wahl, Interplay of ferromagnetism and spin-orbit coupling in  $\text{Sr}_4\text{Ru}_3\text{O}_{10}$ , *Phys. Rev. B* **106**, L241107 (2022).
- [32] C. A. Marques, W. Osmolska, I. Benedičič, L. C. Rhodes, M. Naritsuka, R. Arumugam, V. Granata, R. Fittipaldi, A. Vecchione, and P. Wahl, Symmetry, spin and orbital character of a van-Hove singularity in proximity to a Lifshitz transition in  $\text{Sr}_4\text{Ru}_3\text{O}_{10}$ , [arXiv:2303.05587](https://arxiv.org/abs/2303.05587) (2023).
- [33] G. Cao, S. Chikara, J. W. Brill, and P. Schlottmann, Anomalous itinerant magnetism in single-crystal  $\text{Sr}_4\text{Ru}_3\text{O}_{10}$ : A thermodynamic and transport investigation, *Phys. Rev. B* **75**, 024429 (2007).
- [34] M. Escher, N. B. Weber, M. Merkel, L. Plucinski, and C. M. Schneider, FERRUM: A new highly efficient spin detector for electron spectroscopy, *E-J. Surf. Sci. Nanotechnol.* **9**, 340 (2011).
- [35] See Supplemental Material at <http://> for additional experimental photon-energy dependence, spin-detection details, exchange-correlation functional comparison, and effects of spin-orbit coupling.
- [36] P. Giannozzi, S. Baroni, N. Bonini, M. Calandra, R. Car, C. Cavazzoni, D. Ceresoli, G. L. Chiarotti, M. Cococcioni, I. Dabo, A. D. Corso, S. de Gironcoli, S. Fabris, G. Fratesi, R. Gebauer, et al., QUANTUM ESPRESSO: a modular and open-source software project for quantum simulations of materials, *J. Phys.: Condens. Matter* **21**, 395502 (2009).
- [37] P. Giannozzi, O. Andreussi, T. Brumme, O. Bunau, M. B. Nardelli, M. Calandra, R. Car, C. Cavazzoni, D. Ceresoli, M. Cococcioni, N. Colonna, I. Carnimeo, A. D. Corso, S. de Gironcoli, P. Delugas, et al., Advanced capabilities for materials modelling with quantum ESPRESSO, *J. Phys.: Condens. Matter* **29**, 465901 (2017).
- [38] J. P. Perdew, A. Ruzsinszky, G. I. Csonka, O. A. Vydrov, G. E. Scuseria, L. A. Constantin, X. Zhou, and K. Burke, Restoring the density-gradient expansion for exchange in solids and surfaces, *Phys. Rev. Lett.* **100**, 136406 (2008).
- [39] O. Grånäs, I. D. Marco, O. Eriksson, L. Nordström, and C. Etz, Electronic structure, cohesive properties, and magnetism of  $\text{SrRuO}_3$ , *Phys. Rev. B* **90**, 165130 (2014).
- [40] P. Rivero, V. Meunier, and W. Shelton, Half-metallic ferromagnetism in  $\text{Sr}_3\text{Ru}_2\text{O}_7$ , *Phys. Rev. B* **95**, 195106 (2017).
- [41] Y. Fu and D. J. Singh, Density functional methods for the magnetism of transition metals: SCAN in relation to other functionals, *Phys. Rev. B* **100**, 045126 (2019).
- [42] D. Pappas, K.-P. Kämper, B. Miller, H. Hopster, D. Fowler, C. Brundle, A. Luntz, and Z.-X. Shen, Spin-dependent electron attenuation by transmission through thin ferromagnetic films, *Phys. Rev. Lett.* **66**, 504 (1991).
- [43] H. F. Yang, Z. T. Liu, C. C. Fan, Q. Yao, P. Xiang, K. L. Zhang, M. Y. Li, H. Li, J. S. Liu, D. W. Shen, and M. H. Jiang, Origin of the kink in the band dispersion of the ferromagnetic perovskite  $\text{SrRuO}_3$ : Electron-phonon coupling, *Phys. Rev. B* **93**, 121102(R) (2016).

# *Supplementary Materials for:* Spin-resolved electronic structure of ferromagnetic triple-layered ruthenate $\text{Sr}_4\text{Ru}_3\text{O}_{10}$

Prosper Ngabonziza,<sup>1,2</sup> Jonathan D. Denlinger,<sup>3</sup> Alexei V. Fedorov,<sup>3</sup>  
Gang Cao,<sup>4</sup> J. W. Allen,<sup>5</sup> G. Gebreyesus,<sup>6</sup> and Richard M. Martin<sup>7,8</sup>

<sup>1</sup>*Department of Physics and Astronomy, Louisiana State University, Baton Rouge, LA 70803, USA*

<sup>2</sup>*Department of Physics, University of Johannesburg,*

*P.O. Box 524 Auckland Park 2006, Johannesburg, South Africa*

<sup>3</sup>*Advanced Light Source, Lawrence Berkeley National Laboratory, Berkeley, California 94720, USA*

<sup>4</sup>*Department of Physics, University of Colorado at Boulder, Boulder, Colorado 80309, USA*

<sup>5</sup>*Randall Laboratory of Physics, University of Michigan, Ann Arbor, Michigan 48109, USA*

<sup>6</sup>*Department of Physics, School of Physical and Mathematical Sciences,*

*College of Basic and Applied Sciences, University of Ghana, Ghana*

<sup>7</sup>*Department of Physics, University of Illinois at Urbana-Champaign, Urbana, Illinois 61801, USA*

<sup>8</sup>*Department of Applied Physics, Stanford University, Stanford, California 94305, USA*

## Contents

SM1. Spin-integrated ARPES photon dependence	1
SM2. Spin-resolved ARPES detection	2
SM3. Exchange functional comparison	4
SM4. Spin-orbit coupling	6
SM5. Thin film $\text{SrRuO}_3$ spin-ARPES comparison	7

## SM1 Spin-integrated ARPES photon dependence

Spin-integrated photon-dependent mapping of the electronic structure, both at normal emission and off-normal, was key to the identification of the  $k$ -space locations at which the narrow flat bands at  $\Gamma$  and at the tetragonal BZ boundary saddle-point were strongest intensity and most suitable for subsequent spin-resolved measurements. Figure S1(a) shows a normal emission (first BZ)  $E_F$ -intensity map for LH polarization in which *no* photon energy in the range of 30-124 eV exhibits a strong matrix element enhancement of the  $\Gamma$ -point flat band. In contrast for LV polarization photon-dependent mapping, a strong enhancement centered on 76 eV is observed in Fig. S1(b). However, since LV polarization was not available at the spin-ARPES beamline 10.0.1, further angle-dependent mapping into the second BZ was explored.

Indeed at 76 eV and using LH polarization for angle-dependent mapping, a strong enhancement of the  $(2\pi,0)$   $\Gamma$ -point narrow band is observed in Fig. 1 of the main text. In addition it reveals a very strong enhancement of the  $(3\pi,0)$  saddle-point region as well as the large square FS contour, both used in the spin-ARPES measurements. To further explore the relative  $(2\pi,0)$  matrix element enhancement, an off-normal photon-dependent map with a constant  $k_{\parallel} = 1.62 \text{ \AA}^{-1}$  centered on the second BZ, was performed. As shown in Fig. S1(c), an even greater enhancement was discovered at 56 eV, using LH polarizatin, which also coincidentally corresponded to the maximum flux performance of

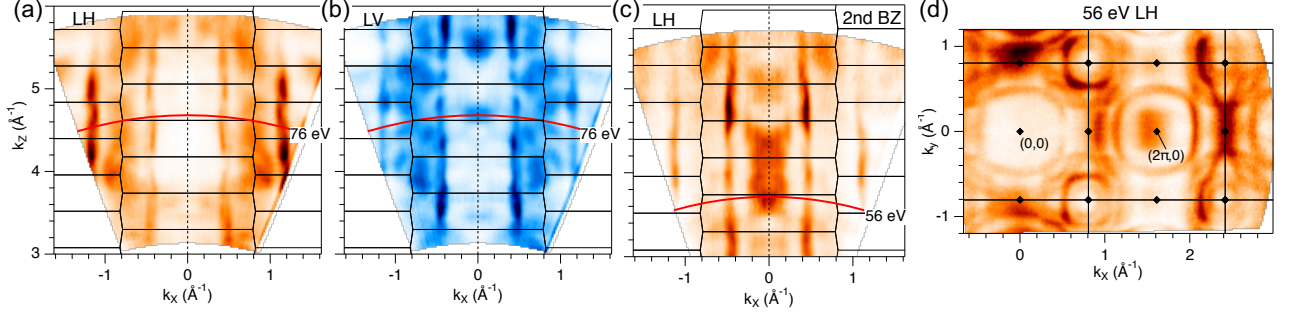


FIG. S1. **Photon energy dependent  $k_x$ - $k_z$  maps.** (a) Normal emission map using LH polarization. (b) Normal emission map using LV polarization. (c) Off-normal second BZ map using LH polarization. (d) Angle-dependent FS map at 56 eV using LH polarization.

the spin-ARPES beamline. Thus 56 eV could be chosen to optimize the  $(2\pi,0)$   $\Gamma$ -point spin-ARPES measurements without having to compromise the energy resolution settings that are very comparable to those at ALS beamline 4.0.3. Figure S1(d) shows the corresponding angular dependent  $k_x$ - $k_z$  FS map at 56 eV showing the  $(2\pi,0)$  second BZ center enhancement of the  $\Gamma$  flat band.

The strong matrix element enhancements observed above originate from ARPES structure factor terms and not from any resonant photoemission process, such as in the f-electron spectra of rare-earth materials tuned to specific 4d-4f absorption edges. Hence we regard the extremely enhanced low temperature spectral weight of the narrow bands at  $(0,0)$  and  $(\pi,0)$ -equivalent points as reflecting true high densities of states, and not an artificial enhancement of the photoemission process that deviates from theoretical predictions (such as DMFT spectral functions). E.g. the absence or weaker appearance of the narrow bands at other  $(0,0)$  and  $(\pi,0)$ -equivalent points reflects a matrix-element *suppression* of spectral weight that deviates from the true DOS.

## SM2 Spin-resolved ARPES detection

Spin-resolved ARPES was measured at the Advanced Light Source beamline 10.0.1 using a Scienta R4000 spectrometer equipped with DA30 deflector plates for spin-integrated ARPES mapping and for steering electrons into dual very low energy electron diffraction (VLEED) spin-detectors. The two exchange-scattering type spin-detectors use in-plane magnetization of FeO thin film targets to provide  $(k_z, k_x)$  and  $(k_z, k_y)$  components of the spin-asymmetry, e.g. with redundancy in the  $k_z$  component. For each spin-detector, the sequentially measured spectra  $I_+(\omega)$  and  $I_-(\omega)$  are used to compute the raw spin-scattering asymmetry,  $A_{\pm}(\omega) = (I_+ - I_-)/(I_+ + I_-)$ , which is corrected by the instrumental spin-scattering efficiency factor, i.e. the Sherman function  $S_{eff}$ , to determine the photoelectron spin-polarization  $P(\omega) = A_{\pm}(\omega)/S_{eff}$ . The corrected spin-dependent spectra are then calculated as  $I_{\uparrow\downarrow}(\omega) = I_{av}(\omega)(1 \pm P(\omega))$ , where  $I_{av} = (I_+ + I_-)/2$ . The Sherman function for this exchange spin-detector is calibrated to be  $S_{eff} \approx 0.25$ .

To achieve uniform magnetic domain alignment for spin-resolved ARPES, a permanent magnet with  $\approx 0.2$  T field strength at the sample surface was used to field-cool the sample, both prior to and after sample cleaving. The magnetization profiles of  $\text{Sr}_4\text{Ru}_3\text{O}_{10}$  in Fig. S2(a) shows how such an external field strength parallel to the  $c$ -axis enables magnetization saturation (domain alignment) of the sample (even without field cooling) and how the magnetization is maintained when the external field is removed. In contrast, the high-moment state for ab-plane

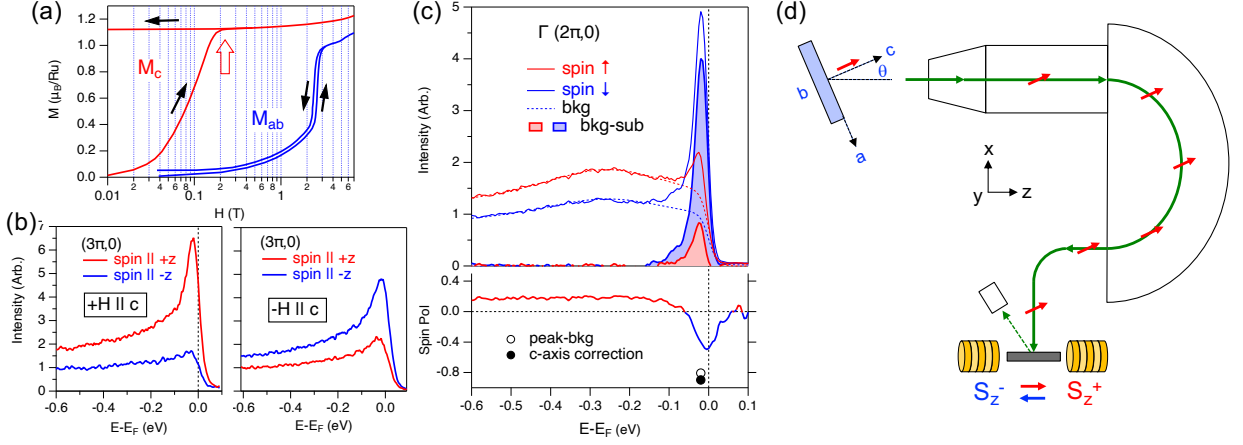


FIG. S2. **Spin-detection procedure and analysis corrections.** (a) Magnetization profile of  $\text{Sr}_4\text{Ru}_3\text{O}_{10}$  at  $T=1.8\text{K}$  [1] illustrating low temperature  $c$ -axis magnetization domain alignment with  $\sim 0.2$  T applied external field. (b) Demonstration of the sign reversal of the experimental spin-spectra for a reversal of the  $c$ -axis external field. (c) Example of background subtractions of the  $\Gamma$ -point narrow peak resulting in enhanced spin-polarization asymmetry (open dot). (d) Schematic of the  $c$ -axis spin-alignment relative to a  $z$ -axis spin-component detection, resulting in an additional  $1/\cos\theta$  spin-polarization correction (solid dot in (c)).

magnetization requires a higher critical field and is not maintained at low temperature. For this study, only a field alignment parallel (or anti-parallel) to the crystalline  $c$ -axis was used, and only the  $k_z$ -components of the spin-asymmetry parallel to this magnetization axis are presented. Fig. S2(b) demonstrates how the sign of the detected spin-asymmetry is reversed if the sample is remagnetized with the external field reversed to be antiparallel to the  $c$ -axis.

The spin-polarization of coherent peaks in the spin-dependent spectra requires additional modeling and subtraction of spin-dependent incoherent background profiles. Fig. S2(c) shows an example of such a procedure to separate out first the coherent peaks (shaded) whose amplitudes (or areas) are then used to compute a single spin-polarization value (open dot). An enhancement of the experimental spin-polarization from 50% to 80% is observed for the  $(2\pi,0)$  example. The spin-polarization of the  $(3\pi,0)$  narrow peak is similarly enhanced to  $>80\%$ , with subtraction of its same-sign majority-spin background.

A second quantitative spin-polarization correction arises from the large  $\sim 26^\circ$ - $34^\circ$  sample polar angles (rotation about the sample vertical  $b$ -axis) required to measure at the second BZ  $(2\pi,0)$  and  $3\pi,0$  points at 56 eV and 76 eV, respectively. The  $P_z$  spin-polarization is not purely aligned to the sample magnetization axis, as shown in Fig. S2(d), but also has a non-zero in-plane component, i.e.  $P_z = P_c \cos\theta + P_a \sin\theta$ . Conversely, a  $P_x$  spin-polarization measurement could contain a non-zero  $c$ -axis component, i.e.  $P_x = -P_c \sin\theta + P_a \cos\theta$ . Hence, a pure  $c$ -axis sample spin-alignment ( $P_a=P_b=0$ ), could result in a non-zero  $P_x$  measurement, and  $P_z$  should be corrected by  $P_c = P_z/\cos\theta$  to obtain the true  $c$ -axis spin-polarization, e.g.  $P_c=1.11P_z \sim 90\%$  for the  $(2\pi,0)$  coherent peak in Fig. S2(c).

### SM3 Exchange functional comparison

In Fig. S3, we provide a side-by-side comparison of three spin-polarized DFT calculations with different nominal exchange splittings of approximately 0.6, 0.9 and 1.1 eV. The PBEsol and PBEsol+U (1eV) bands are taken from Ref. [2] and replotted with left/right separation of spin-up/down states for greater clarity. The octahedral rotation and zone-folding effect, indicated by the (0,0) and  $(\pi,\pi)$  labeling equivalence, has not been unfolded to the tetragonal BZ (as performed in Fig. 3(a)). The LDA functional calculation, new to this work, is similarly plotted. A recent PBE96 calculation from Benedičić et al.[3] also predicts a large exchange splitting value of  $\sim 1.1$  eV similar to the PBEsol+U calculation, in which the Fermi-level cuts just slightly below the highest energy  $(\pi,\pi)$  hole band.

The better agreement of the LDA functional to experiment, the systematic trend towards increasing exchange splitting and larger moments for LDA  $\rightarrow$  PBEsol  $\rightarrow$  PBE96  $\rightarrow$  DFT+U, and the prediction of a large moment half-metal groundstate for small U is consistent with previous comparative studies of DFT exchange-correlation functionals for magnetism in SrRuO<sub>3</sub> [4], Sr<sub>3</sub>Ru<sub>2</sub>O<sub>7</sub> [5] and FM transition metals [6].

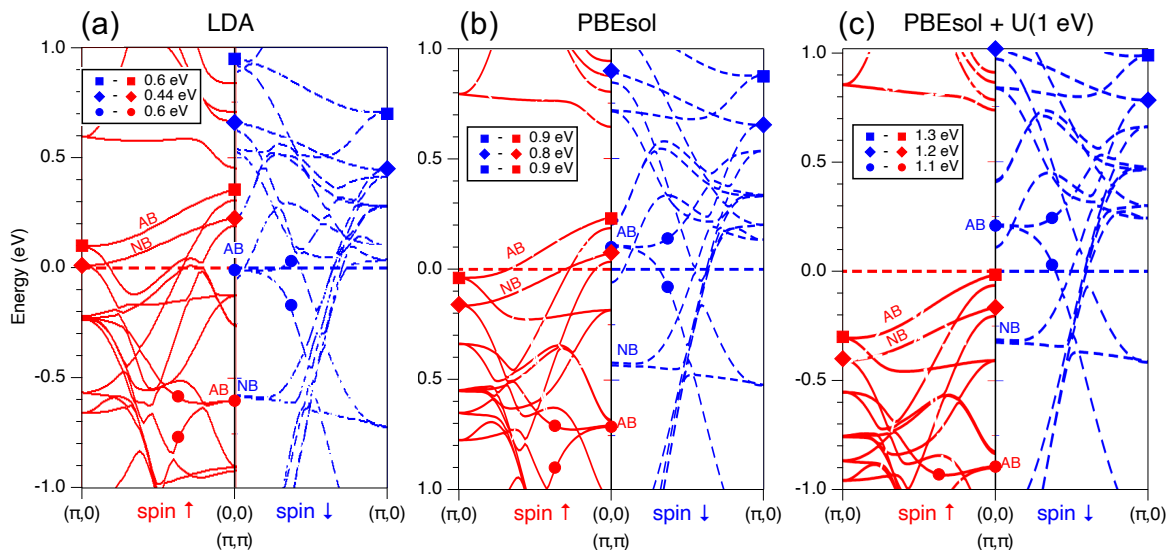


FIG. S3. **Comparison of different exchange-correlation functionals** Spin-polarized Sr<sub>4</sub>Ru<sub>3</sub>O<sub>10</sub> for three different (a) LDA (b) PBEsol and (c) PBEsol + U (1 eV). The  $E_F$  result in (c) is very similar to a recent PBE96 calculation [3]. Round, diamond and square symbols help to identify key equivalent spin-up and spin-down bands for purpose of evaluating the exchange splitting variations.

The comparison in Fig. S3 also highlights the main text logic flow for the variable exchange-splitting exercise to find a consistent assignment of both the -30 meV narrow hole band at (0,0) and the saddle-point band at  $(\pi,0)$ , as well as find a quantitative agreement with the  $(\pi,\pi)$  hole FS contours.

(i) The large DFT+U exchange splitting result in Fig. S3(c) of a half-metal in which the spin-majority states are completely filled is trivially ruled out due to the distinct experimental observation of spin-majority FS contours in the  $(\pi,\pi)$  region. This also rules out an NB  $d_{xy/yz}$  flat band origin for the narrow hole-like state at (0,0) which would require an even larger upwards spin-down energy shift and/or extremely large  $>10\times$  energy renormalizations to achieve a -30 meV energy.

(ii) With the spin-minority AB flat state at (0,0) being the target assignment of the strong ARPES at (0,0), the

PBEsol calculation to PBEsol calculation in Fig. S3(c) is observed to incorrectly predict the spin-minority AB state to reside just *above*  $E_F$ . Also, while a shallow AB-derived spin-majority saddle-point band is correctly predicted to be below  $E_F$  at  $(\pi,0)$ , it also predicts a second parallel dispersing NB-derived saddle-point band to be just below it. In contradiction, ARPES shows only *one* -30 meV saddle-band dispersion.

(iii) A reduced overall exchange-splitting is proposed that both lowers the spin-minority AB state to be below  $E_F$ , and raises the spin-majority states to produce only a single NB-derived saddle-point dispersion below  $E_F$ . Rigid shift corrections of +0.10 (-0.16) eV to the PBEsol spin-up (down) bands are selected, i.e. total exchange splitting of 0.64 eV ( $\approx 0.9-0.26$ ). The spin-up correction is fine-tuned to provide a quantitative match to the three (flower + two nested square) FS contours at  $(\pi,\pi)$ . The large velocity spin-minority  $d_{xy}$  electron bands that form the large squarish contour(s) centered on  $(0,0)$  are less sensitive to the small corrections to the exchange splitting. Also consistent with ARPES, another  $d_{xy/yz}$  NB-derived light mass band converges with the  $d_{xy}$  band near  $E_F$ .

(iv) The LDA functional calculation in Fig. S3(a) also predicts a smaller exchange splitting of  $\sim 0.6$  eV in closer agreement to the ARPES-matching PBEsol exchange-splitting adjustment. A rigid shift correction of -0.05 (-0.05) eV to the LDA spin-up (down) bands is required to obtain a similar result to the PBEsol exchange-splitting correction.

(v) The PBEsol and LDA calculations without spin-orbit coupling (SOC) predict two-fold band degeneracies of the B, NB and AB  $d_{xy/yz}$  states at  $(0,0)$ . When the degenerate AB state is shifted to be below  $E_F$  to obtain agreement with the experimental shallow hole band at  $(0,0)$ , this results in the prediction of an upwards dispersing electron-like  $E_F$ -crossing that is not observed experimentally. This discrepancy is cured by the inclusion of SOC which splits this degeneracy at  $(0,0)$  as illustrated in the next supplemental section SM4.

(vi) The main text discusses the comparison of the average magnetic moment ( $M_{tot}/3$ ) of the PBEsol and LDA calculations to the experimental  $\text{Sr}_4\text{Ru}_3\text{O}_{10}$  low temperature saturated moment of  $1.1 \mu_B/\text{Ru}$  for low-field c-axis magnetization [1]. The moment increases to  $1.2 \mu_B/\text{Ru}$  at higher applied fields of 7 T. Larger experimental total moments up to  $1.36 \mu_B/\text{Ru}$  have been reported [7], but are likely the result of contamination by ingrowth of  $\text{SrRuO}_3$ -like higher-order ruthenate layers [8] which giving an additional  $M \sim 0.2$  contribution extending above  $T_c = 105$  K up to 160 K, i.e. the Curie temperature for  $\text{SrRuO}_3$ . Table S1 summarizes these moment and exchange splitting values.

TABLE S1. Comparison of experimental and spin-polarized DFT calculated exchange splittings and average magnetic moments.

Exchange-Correlation Functional	Exchange Splitting (eV)	Average Moment <sup>a</sup> ( $\mu_B/\text{Ru}$ )	Reference
LDA (unrelaxed)	0.44-0.6	1.36	-
LDA (relaxed)	0.44-0.6	1.17	-
PBEsol	0.8-0.9	1.77	[2]
PBE96	1.1	- <sup>b</sup>	[3]
PBEsol+U(1 eV)	1.1-1.3	$\sim 2$	[2]
LDA+U(2 eV)	1.1-1.3	$\sim 2$	-
Energy-shifted PBEsol	0.64	-	$\approx$ ARPES
Experiment, B  c, 0.1T	-	1.1	[1]
Experiment, B  c, 7T	-	1.2	[1]

<sup>a</sup>  $M_{av} = M_{tot}/3$ . <sup>b</sup> value not reported.

## SM4 Spin-orbit coupling

We have ignored spin-orbit coupling (SOC) in much of the analysis since it is mainly a small effects and it complicates the analysis in terms of majority- and minority-spins. However, it is important for details of the bands near the Fermi energy. The DFT PBEsol calculations without SOC presented in Fig. 3(b) predict two extraneous features (highlighted by yellow arrows) that are not experimentally observed. (i) The PBEsol predicts two-fold band degeneracies of the B, NB and AB  $d_{xy/yz}$  states at  $(0,0)$ , which result in the prediction of both downwards and upwards dispersing branches from the AB state. Thus, after correcting the AB to be below  $E_F$ , an electron-like  $E_F$ -crossing is predicted which is not observed experimentally. (ii) In addition, the bottom of spin-minority states at  $(\pi,0)$  are only  $\sim 20$  meV higher than the  $(0,0)$  AB state energy. Thus, the AB energy correction inevitably also shifts these spin-minority states to be crossing below  $E_F$  at  $(\pi,0)$  – which are also not experimentally observed.

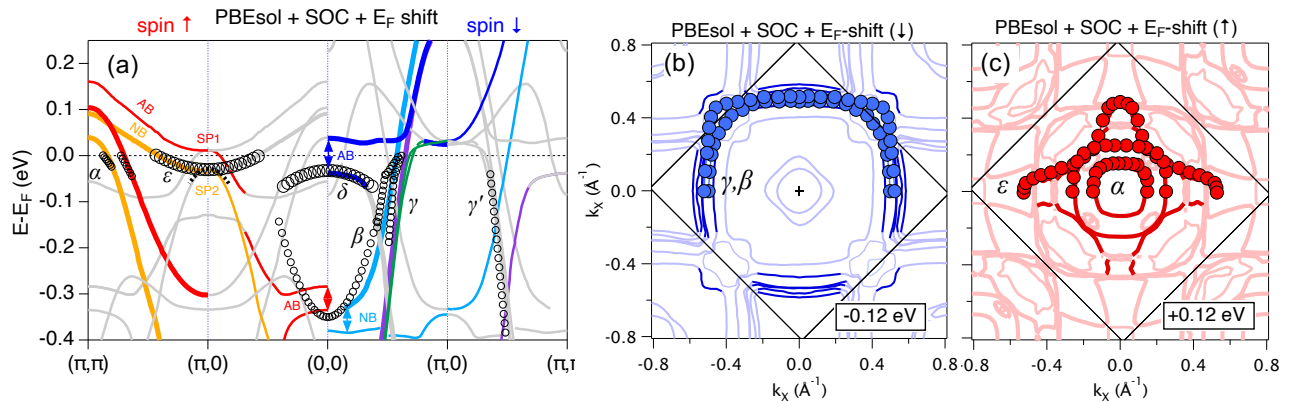


FIG. S4. **PBEsol + Spin-orbit Coupling comparison to ARPES.** (a) Energy-shifted and scaled PBEsol+SOC bands with  $\approx 0.6$  eV exchange splitting, giving similar  $(\pi,\pi)$  and  $(\pi,0)$  spin-majority agreement to ARPES as in Fig. 3(b), but with key SOC-splitting of the spin-minority AB band degeneracy at  $(0,0)$ . (b) Experimental spin-minority FS contours ( $\gamma/\beta$ ) compared to energy-shifted PBEsol+SOC FS contours. Lighter shaded contours correspond to zone-folded bands. (c) Experimental spin-majority FS contours ( $\alpha, \epsilon$ ) compared to energy-shifted PBEsol+SOC FS contours. Many of the lighter shaded contours correspond to spin-minority bands (with incorrect energy shifts) due to finite spin-mixing in the SOC calculation.

As shown by the DFT calculations [2], SOC splits the  $d_{xy/yz}$  state degeneracies at  $(0,0)$  and creates two separated electron-like and hole-like narrow AB bands with even flatter band dispersions near  $(0,0)$ . Reduction of the exchange splitting so that  $E_F$  lies in this spin-minority SOC gap, as shown in Fig. S4(a), preserves the AB energy level and renormalized dispersion agreement to ARPES, while eliminating the unobserved electron branch. In addition, SOC pushes the bottom of the spin-majority states at  $\pi,0$  to higher energy above  $E_F$  in alignment with the upper AB branch at  $(0,0)$ . This also cures the PBEsol presence of spin-minority FS contours in the  $(\pi,0)$  region of Fig. 3(c), which are now absent in Fig. S4(b). A symmetric rigid shift correction  $+0.12$  ( $-0.12$ ) eV to the PBEsol+SOC spin-up (down) bands also gives similar agreement as PBEsol (without SOC) to the  $(\pi,\pi)$  region FS contours [Fig. S4(c)].

A final observation from both the shifted and scaled PBEsol plot in Fig. 3(b) and the PBEsol+SOC plot in Fig. S4(a) is that the lack of experimental spin-polarization of the bottom of the experimental  $\beta$  band at  $(0,0)$ , i.e. the  $0.2$  eV wide spectral hump centered at  $-0.35$  eV in Fig. 2(a), originates from the coincidental energy alignment of downwards-shifted spin-majority AB states and upwards-shifted spin-minority NB states. The SOC splitting of these states contributes to the broadened width of the experimental spectral hump.

## SM5 Thin film SrRuO<sub>3</sub> spin-ARPES comparison

Similarities and differences between a recent spin-ARPES study of a 15 unit-cell thin film of SrRuO<sub>3</sub> [9] and our study of cleaved bulk Sr<sub>4</sub>Ru<sub>3</sub>O<sub>10</sub> crystals are discussed.

(1) **(0,0) hole-band.** A shallow hole-like band very close to  $E_F$  is observed at the zone center  $\Gamma$ -point in both systems. In the SrRuO<sub>3</sub> thin film study, the hole band maximum is at -10 meV and has a relatively stronger intensity than the other FS crossing bands for the 21.2 eV measurement. Its existence in SrRuO<sub>3</sub> is identified as originating from one of the *two* operative zone-foldings from octahedral rotations and tilting distortions, and is labeled  $\alpha'$  indicating  $(\pi,\pi)$  origins. Also it has the same majority spin-polarization as the high binding energy background, with the corresponding spin-minority hole-band identified in the spin-integrated spectra as crossing  $E_F$  with a 32 meV exchange-splitting.

In contrast, the zone center flat band in Sr<sub>4</sub>Ru<sub>3</sub>O<sub>10</sub> has a band maximum of -30 meV, and has a dramatically strong intensity at low  $T$  (for the optimized photon energy in the second BZ). It is identified in this study to originate from the spin-minority trilayer-split  $d_{xy/yz}$  AB flat band in DFT, and hence it exists regardless of octahedral rotations and zone-folding. Sharp zone-folded  $(\pi,\pi)$  hole-bands are separately observed at (0,0).

(2) **Spin-split band pairs.** In the thin film SrRuO<sub>3</sub> study, spin-split parallel dispersing bands are identified for the (0,0) hole band and also for a large rounded-square  $\beta$  band crossing  $E_F$ . A small *true* exchange energy splitting of  $\sim 0.12$  eV was derived from the 32 meV splitting of the  $\alpha'$  hole band multiplied by a  $3.8\times$  energy renormalization of the  $\beta$  band exhibiting a low energy kink in the band dispersion.

In this Sr<sub>4</sub>Ru<sub>3</sub>O<sub>10</sub> study, we separately observe spin-majority itinerant bands crossing  $E_F$  at  $(\pi,\pi)$  and spin-minority itinerant bands forming the large square FS contours centered on (0,0); however, without observation of the corresponding parallel-dispersing opposite-spin band in either case. This is due to a much larger  $\sim 0.3$  eV exchange splitting determined from the theory-experiment comparison, i.e.  $\sim 0.6$  eV prior to an  $\sim 2\times$  energy renormalization, which is comparable to the bandwidth of the relevant bands involved at the top of the Ru  $d$ - $t_{2g}$  manifold.

(3)  **$T$ -dependent exchange splitting.** A 2013 thin film SrRuO<sub>3</sub> ARPES study [10] did not reveal any significant change in the exchange split band structure up to  $T_c$ . The recent thin film SrRuO<sub>3</sub> study [9] observes a temperature-dependent reduction of the exchange energy splitting of the (0,0)  $\alpha'$  hole band (from 0.12 eV to 0.04 eV at  $T_c$ ) as well as a reduction of the momentum separation of the spin-split  $\beta$   $E_F$ -crossing bands. However, the accompanying increased spectral broadening up to  $T_c$  prevent the authors from definitively distinguishing partial versus full reduction of the exchange splitting.

In Sr<sub>4</sub>Ru<sub>3</sub>O<sub>10</sub> we also observe (not reported here) a variable exchange splitting behavior of a small momentum shift of the  $(\pi,\pi)$  spin-majority bands, accompanied by increasing broadening of the states at  $E_F$  near  $T_c$ . The corresponding spin-majority energy shift of only 50 meV is significantly smaller than the  $\pm 0.15$  eV exchange splitting energy shifts derived from comparison to DFT, and is strongly suggestive of a non-Stoner-like finite exchange splitting remaining at  $T_c$ .

(4) **Spin-majority background.** Common to both studies is the observation of a spin-majority polarization of the mostly featureless high binding energy background. In the thin film SrRuO<sub>3</sub> study, the background spin-polarization

of  $\sim 15\%$ , presented down to  $-0.5$  eV, is interpreted as arising from localized spin-majority Ru- $d$  states based on their DMFT calculations which also predicts a large  $>50\%$  net spin-majority polarization in the incoherent high binding region. In addition, an enhanced spin-majority *inelastic* background for photoelectrons propagating to the surface due to disparate spin-dependent inelastic mean free paths is a well known alternative origin [11].

In this Sr<sub>4</sub>Ru<sub>3</sub>O<sub>10</sub> study, the wide-energy range spectrum Fig. 2(e) exhibits a little larger value of  $\sim 20\%$  net spin-majority polarization, but *only* in the Ru- $d$  valence band region above the oxygen bands. This confirms the *intrinsic* incoherent spectral weight origin of the Ru- $d$  spin-polarized background, with weak or negligible contribution from extrinsic inelastic-scattering energy-loss spectral weight, which should also extend below the oxygen bands.

## References

- [1] G. Cao, L. Balicas, W. H. Song, Y. P. Sun, Y. Xin, V. A. Bondarenko, J. W. Brill, S. Parkin, and X. N. Lin, Competing ground states in triple-layered Sr<sub>4</sub>Ru<sub>3</sub>O<sub>10</sub>: Verging on itinerant ferromagnetism with critical fluctuations, *Phys. Rev. B* **68**, 174409 (2003).
- [2] G. Gebreyesus, P. Ngabonziza, J. Nagura, N. Seriani, O. Akin-Ojo, and R. M. Martin, Electronic structure and magnetism of the triple-layered ruthenate Sr<sub>4</sub>Ru<sub>3</sub>O<sub>10</sub>, *Phys. Rev. B* **105**, 165119 (2022).
- [3] I. Benedičić, M. Naritsuka, L. C. Rhodes, C. Trainer, Y. Nanao, A. B. Naden, R. Fittipaldi, V. Granata, M. Lettieri, A. Vecchione, and P. Wahl, Interplay of ferromagnetism and spin-orbit coupling in Sr<sub>4</sub>Ru<sub>3</sub>O<sub>10</sub>, *Phys. Rev. B* **106**, 1241107 (2022).
- [4] O. Grånäs, I. D. Marco, O. Eriksson, L. Nordström, and C. Etz, Electronic structure, cohesive properties, and magnetism of SrRuO<sub>3</sub>, *Phys. Rev. B* **90**, 165130 (2014).
- [5] P. Rivero, V. Meunier, and W. Shelton, Half-metallic ferromagnetism in Sr<sub>3</sub>Ru<sub>2</sub>O<sub>7</sub>, *Phys. Rev. B* **95**, 195106 (2017).
- [6] Y. Fu and D. J. Singh, Density functional methods for the magnetism of transition metals: SCAN in relation to other functionals, *Phys. Rev. B* **100**, 045126 (2019).
- [7] Z. Xu, X. Xu, R. S. Freitas, Z. Long, M. Zhou, D. Fobes, M. Fang, P. Schiffer, Z. Mao, and Y. Liu, Magnetic, electrical transport, and thermoelectric properties of Sr<sub>4</sub>Ru<sub>3</sub>O<sub>10</sub>: Evidence for a field-induced electronic phase transition at low temperatures, *Phys. Rev. B* **76**, 094405 (2007).
- [8] E. Carleschi, B. P. Doyle, R. Fittipaldi, V. Granata, A. M. Strydom, M. Cuoco, and A. Vecchione, Double metamagnetic transition in Sr<sub>4</sub>Ru<sub>3</sub>O<sub>10</sub>, *Phys. Rev. B* **90**, 205120 (2014).
- [9] S. Hahn, B. Sohn, M. Kim, J. R. Kim, S. Huh, Y. Kim, W. Kyung, M. Kim, D. Kim, Y. Kim, T. W. Noh, J. H. Shim, and C. Kim, Observation of spin-dependent dual ferromagnetism in perovskite ruthenates, *Phys. Rev. Lett.* **127**, 256401 (2021).
- [10] D. E. Shai, C. Adamo, D. W. Shen, C. M. Brooks, J. W. Harter, E. J. Monkman, B. Burganov, D. G. Schlom, and K. M. Shen, Quasiparticle mass enhancement and temperature dependence of the electronic structure of ferromagnetic SrRuO<sub>3</sub> thin films, *Phys. Rev. Lett.* **110**, 087004 (2013).
- [11] D. Pappas, K.-P. Kämper, B. Miller, H. Hopster, D. Fowler, C. Brundle, A. Luntz, and Z.-X. Shen, Spin-dependent electron attenuation by transmission through thin ferromagnetic films, *Phys. Rev. Lett.* **66**, 504 (1991).